Supplementary Materials

Machine learning-driven optimization of plasma-coupled photocatalytic CO_2 reduction system for syngas production

Runze Bi[1,2,#], Tingting Gao[3,#], Yanan Wang[1,4], Dong Wang[5], Huiwen Zhu[6], Ziyun Xi[1,2], Hongling Qin[1,2], Huanyi Wang[7], Ziqi Geng[2], Yijie Yao[2], Yiyong Guan[2], Honglei Zhang[1,2,*]

[1]Nottingham Ningbo China Beacons of Excellence Research and Innovation Institute, Ningbo 315100, Zhejiang, China.

[2]Department of Chemical and Environmental Engineering, The University of Nottingham Ningbo China, Ningbo 315100, Zhejiang, China.

[3]Beilun Branch of Ningbo Municipal Bureau of Ecology and Environment, Ningbo 315800, Zhejiang, China.

[4]Department of Mechanical, Materials and Manufacturing Engineering, The University of Nottingham Ningbo China, Ningbo 315100, Zhejiang, China.

[5]Beijing Perfectlight Technology Co., Ltd., Beijing 100080, China.

[6]College of Digital Technology and Engineering, Ningbo University of Finance & Economics, Ningbo 315175, Zhejiang, China.

[7]School of Materials Science and Chemical Engineering, Ningbo University, Ningbo 315211, Zhejiang, China

[#]These authors contributed equally to this work.

[*]**Correspondence to:** Prof. Honglei Zhang, Nottingham Ningbo China Beacons of Excellence Research and Innovation Institute, Ningbo 315100, Zhejiang, China; Department of Chemical and Environmental Engineering, The University of Nottingham Ningbo China, Ningbo 315100, Zhejiang, China. E-mail: honglei-zhang@nottingham.edu.cn

Experimental equipment and processes

The plasma-photocatalytic CO_2 reduction (P^2CR) experiments were carried out in a custom-built dielectric barrier discharge (DBD) reactor system (Beijing Perfectlight Technology Co., Ltd.), as shown in Supplementary Figure 1. The setup consisted of a square quartz reactor (100×100×50 mm, wall thickness 3 mm), a high-voltage power supply, a 300 W Xe lamp, mass flow controllers (Brooks Instrument, GF40 series), a humidification module, and an online gas-analysis system. The reactor was operated at atmospheric pressure using high-purity CO_2 as the feed gas and Ar as carrier gas, with the CO_2/Ar volume ratio maintained at 1:1 using the mass flow controllers. The total inlet gas flow rate (CO_2+Ar) was varied from 20 to 60 mL min^{-1}, corresponding to a nominal gas residence time of 20–60 s based on the effective discharge volume (about 20 cm^3) defined by the electrode area and the 2 mm discharge gap. The relative humidity was controlled in the range of 32–58%. Before each experiment, stable gas-flow and humidity conditions were established using a temperature-controlled humidification system, and the relative humidity was continuously monitored using a hygrometer (OHR-WS50R-S3-D1-G1-01-A). During operation, the reactor was connected to an external circulating water-cooling system maintained at 30 °C to reduce bulk temperature fluctuations. The outer surface temperature of the reactor was monitored using an infrared thermal imaging camera (Testo 868) to qualitatively assess the thermal effect induced by plasma discharge and light irradiation. In the reaction zone, certain amount of photocatalyst was uniformly distributed over the bottom-electrode region of the reactor. DBD plasma was generated with a fixed electrode gap of 2 mm, while continuous irradiation from a 300 W Xe lamp (PLS-SXE300D/300DUV, Beijing Perfectlight) was introduced vertically from the top of the reactor without an optical filter, with a lamp-to-catalyst distance of 10 cm. The nominal incident light intensity was varied from 600 to 1400 mW cm^{-2}. The electrical characteristics of the discharge were recorded using a Tektronix TBS2000 oscilloscope equipped with a high-voltage probe (Tektronix P5200A) and a high-frequency current probe (Tektronix CT1F). The plasma was operated at a fixed frequency of 10 kHz, and the discharge condition was adjusted by varying the applied voltage from 10 to 50 V. Before catalytic testing, each gas chromatographic (GC) system was calibrated independently using certified standard gas mixtures within its own validated linear response range. For the plasma-catalytic and plasma-photocatalytic experiments, where the gaseous product concentrations were relatively high, gas products were analysed using a conventional GC system (GC-8090PLUS) equipped with thermal conductivity detector (TCD) and flame ionization detector (FID) modules (100 ppm detection threshold). The quantification of H_2, CO, and CO_2 was based on the TCD response, whereas the FID channel was used only to screen for possible hydrocarbons and oxygenated organic byproducts. For the light-only photocatalytic experiments, because the CO concentration was substantially lower than that observed under plasma-only and plasma-photocatalytic conditions, trace CO was quantified using a dedicated high-sensitivity GC system (GC-7090II). In this system, CO was first catalytically converted and then detected by FID, enabling reliable trace-CO analysis in the low-concentration regime (1 ppm detection threshold). A separate calibration curve for trace CO was established for this analytical channel using certified standard gas mixtures in the corresponding low-concentration range. Product concentrations were obtained by converting detector peak areas using the corresponding calibration curves of each instrument. For each catalyst, control experiments were conducted using the same catalyst loading and feed-gas composition. All experiments were independently repeated three times.

To evaluate the performance of the photocatalyst, the yield of the products and the conversion rate of the reactants are calculated by using the following formulas.

The conversion of CO_2:[1]

$$X_{CO_2}(\%) = \frac{CO_2\ input - CO_2\ output}{CO_2\ input} \times 100 \qquad (1)$$

The yield of product gas:[2]

$$Yield_{CO\ or\ H_2}(mmol\ g^{-1}\ h^{-1}) = \frac{n_{CO\ or\ H_2}}{Weight\ of\ catalyst} \times 60 \quad (2)$$

where, $n_{CO\ or\ H_2} = \frac{F \times V}{22.4}$, F is gas flow rate (mL min^{-1}). V is the measured concentration of the product gas (vol.%). In Eq. (2), V is divided by 100 to convert vol.% to a dimensionless volume fraction.

Photocatalyst preparation

Cu–Pd/TiO_2 photocatalysts were synthesized via a conventional wet impregnation method. The total metal loading was fixed at 5 wt% relative to TiO_2. In a typical procedure, 1.0 g of TiO_2 powder was dispersed in deionized water and ultrasonicated to obtain a homogeneous suspension. Aqueous solutions of copper nitrate trihydrate and palladium nitrate were separately prepared to achieve a Cu:Pd metal molar ratio of 1:1, followed by ultrasonic treatment and subsequent mixing to form a uniform metal precursor solution. The prepared precursor solution was then introduced dropwise into the TiO_2 suspension under continuous ultrasonication to ensure uniform dispersion of metal species on the support. The resulting mixture was further stirred and aged at room temperature to facilitate sufficient metal precursor adsorption onto the TiO_2 surface. Subsequently, the sample was dried under vacuum at 100 °C to remove residual solvent and finally calcined in air at 500 °C to obtain the Cu–Pd/TiO_2 photocatalyst.

Low–High Pairwise Interaction Screening

A low–high 2×2 model-based screening was performed to evaluate the conditional dependence between pairs of operating variables. For each variable pair, the two selected variables were set to their experimentally observed lower and upper levels, while the remaining variables were fixed at representative central conditions: discharge power of 50 W, catalyst dosage of 40 mg, gas flow rate of 40 mL min^{-1}, relative humidity of 40%, and light intensity of 1000 mW cm^{-2}. The conditional interaction contrast was calculated as follows:

$$Interaction\ contrast = Y_{high,high} - Y_{low,high} - Y_{high,low} - Y_{low,low} \qquad (3)$$

where Y represents the model-predicted output. A positive value indicates that the combined high-level condition produces a response higher than the additive expectation, whereas a negative value indicates a response lower than the additive expectation. This screening is exploratory and represents model-predicted conditional relationships rather than a factorial experiment or direct evidence of reaction mechanisms.

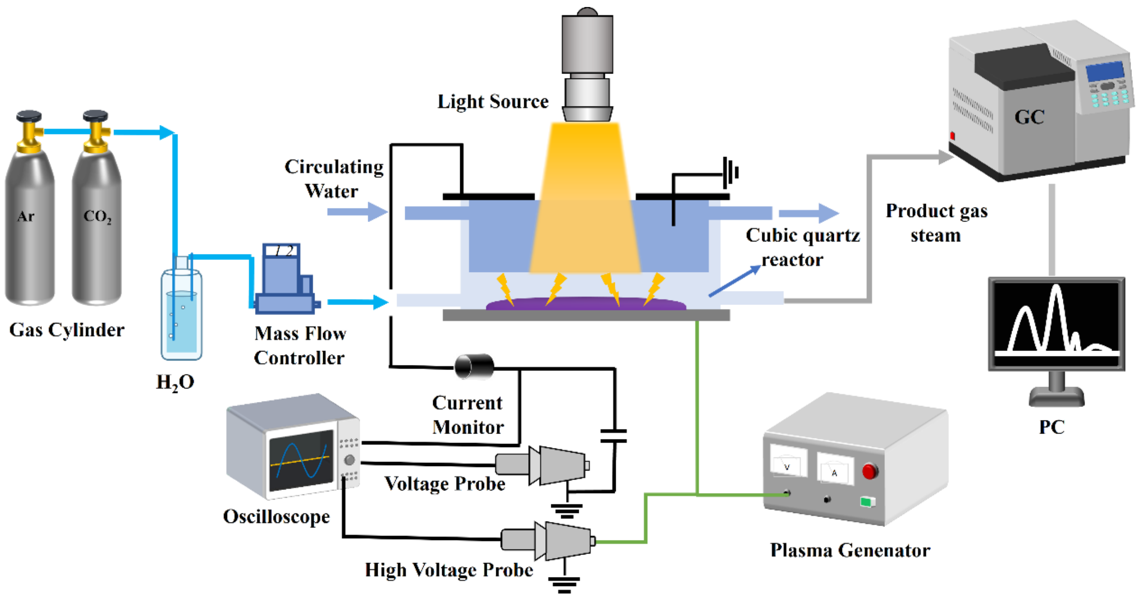

Supplementary Figure 1. Scheme of P^2CR system.

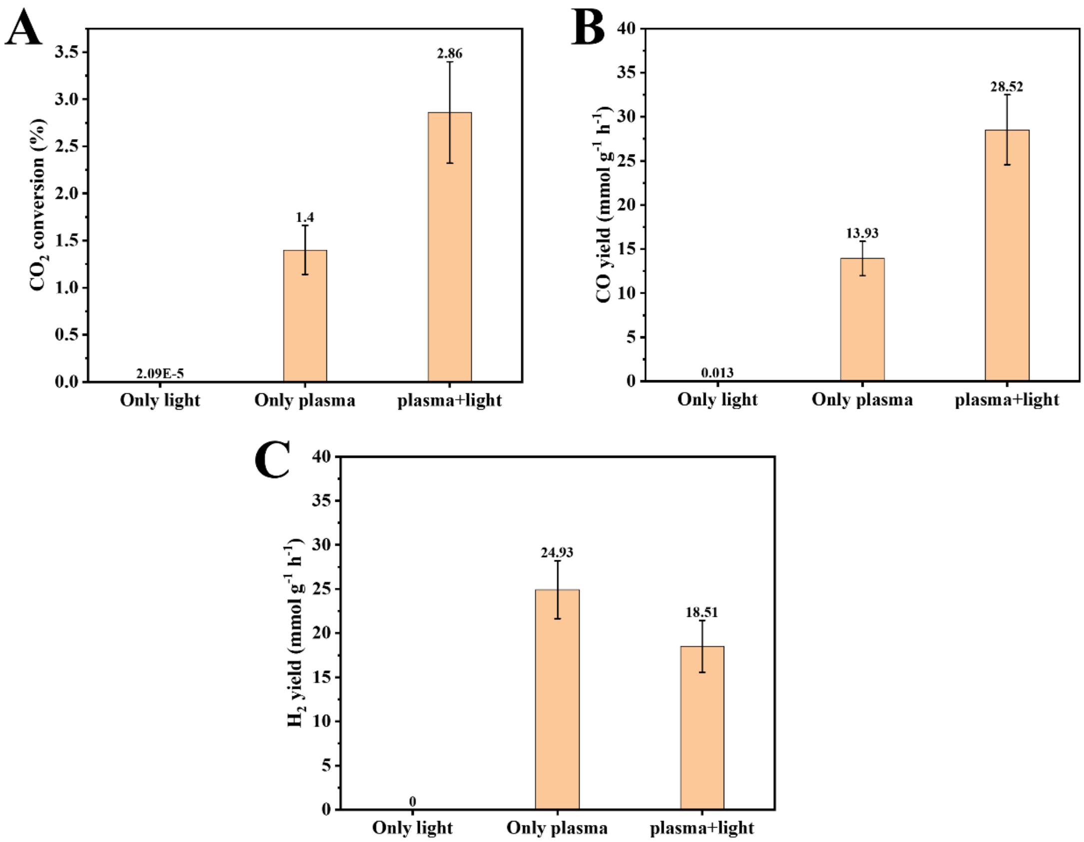

Supplementary Figure 2. Catalytic performance of (A) CO_2 conversion, (B) CO yield and (C) H_2 yield of Cu–Pd/TiO_2 under only-light, only-plasma and plasma–light coupling conditions, respectively. (Discharge power: 60 W, catalysts dose: 30 mg, gas flow: 30 mL min^{-1}, relative humidity 50%, light intensity: 1000 mW cm^{-2}).

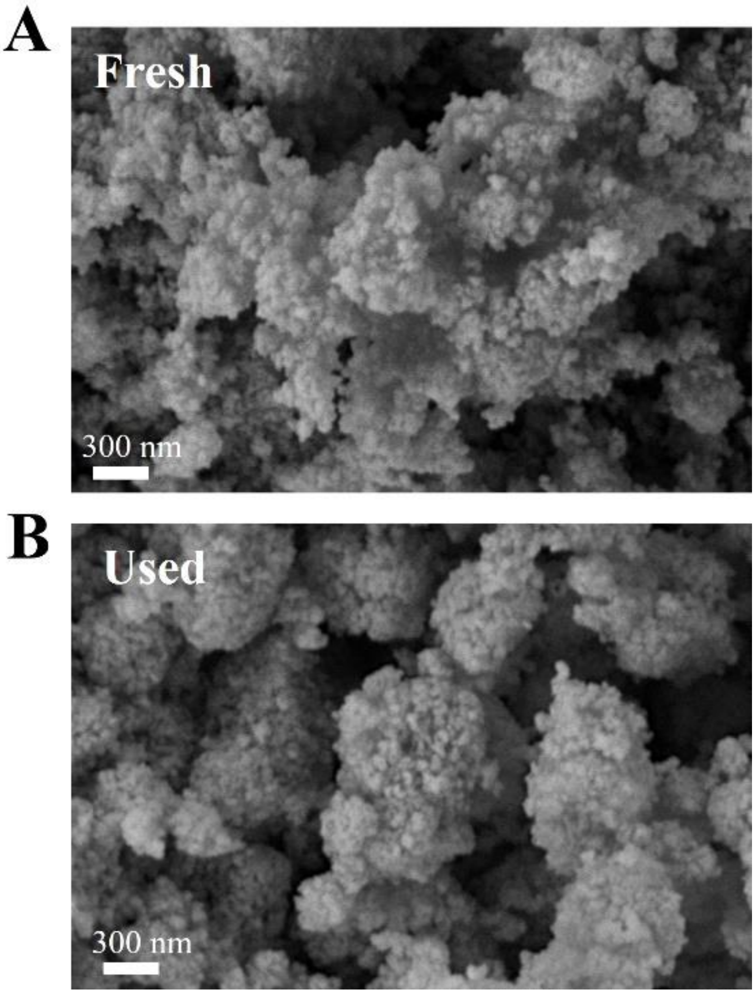

Supplementary Figure 3. SEM images of (A) fresh and (B) used Cu–Pd/TiO_2.

SEM images of fresh and used Cu–Pd/TiO_2 catalysts are shown in Supplementary Figure 3. After catalytic reaction, the used catalyst maintains a similar particle aggregation structure without obvious collapse or severe sintering, suggesting good structural stability during the photocatalytic process.

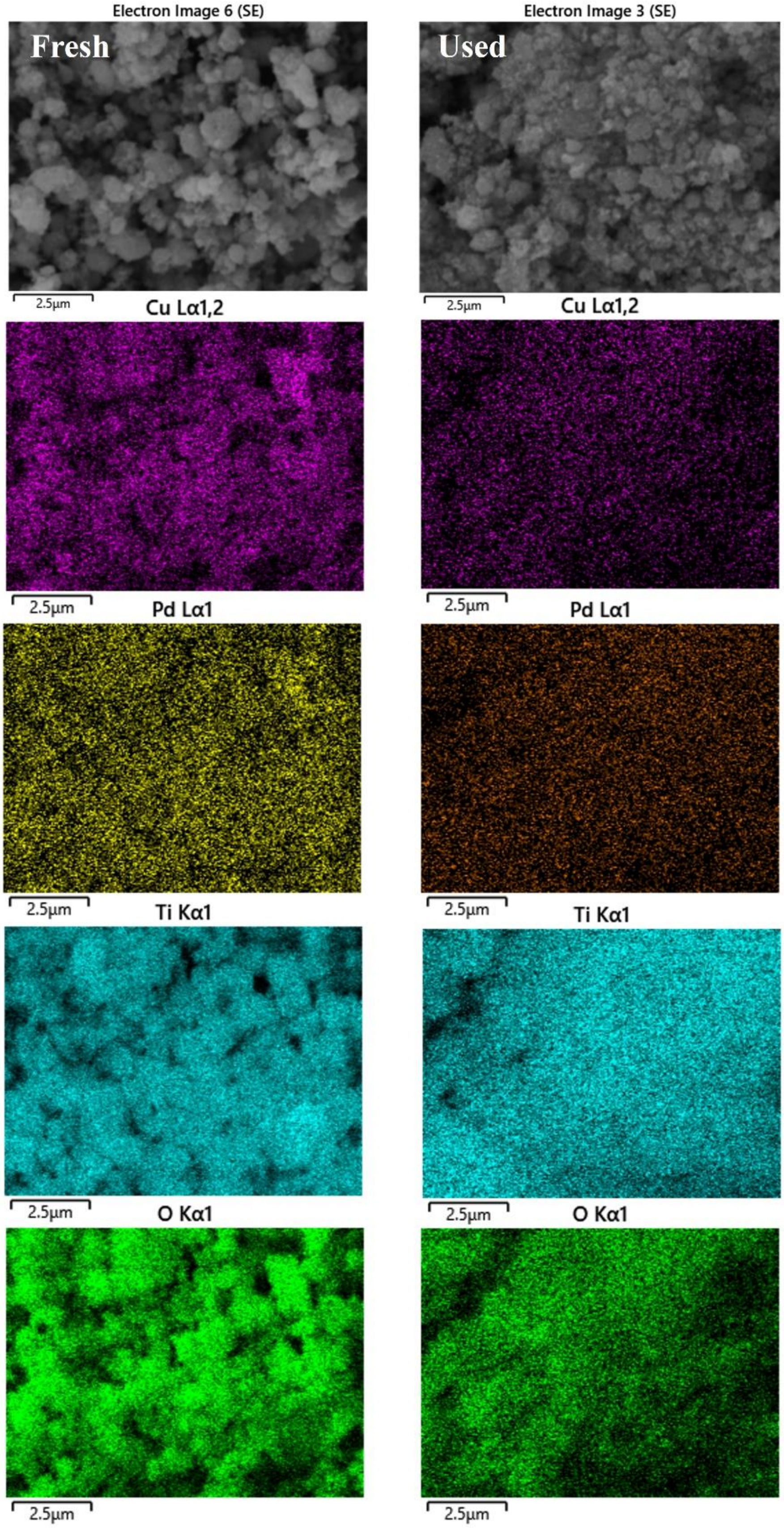

Supplementary Figure 4. The EDS mapping of fresh and used Cu–Pd/TiO_2 photocatalyst.

The elemental mapping results demonstrate the homogeneous distribution of Cu, Pd, Ti, and O elements throughout both fresh and used Cu–Pd/TiO_2 catalysts. The uniform dispersion of Cu and Pd species indicates that the noble metal and transition metal components are successfully anchored onto the TiO_2 support rather than forming largely isolated aggregates. After reaction, the elemental distributions remain almost unchanged, confirming that Cu and Pd species are not significantly leached during the catalytic process. The preserved elemental dispersion contributes to the excellent catalytic durability of the Cu–Pd/TiO_2 catalyst.

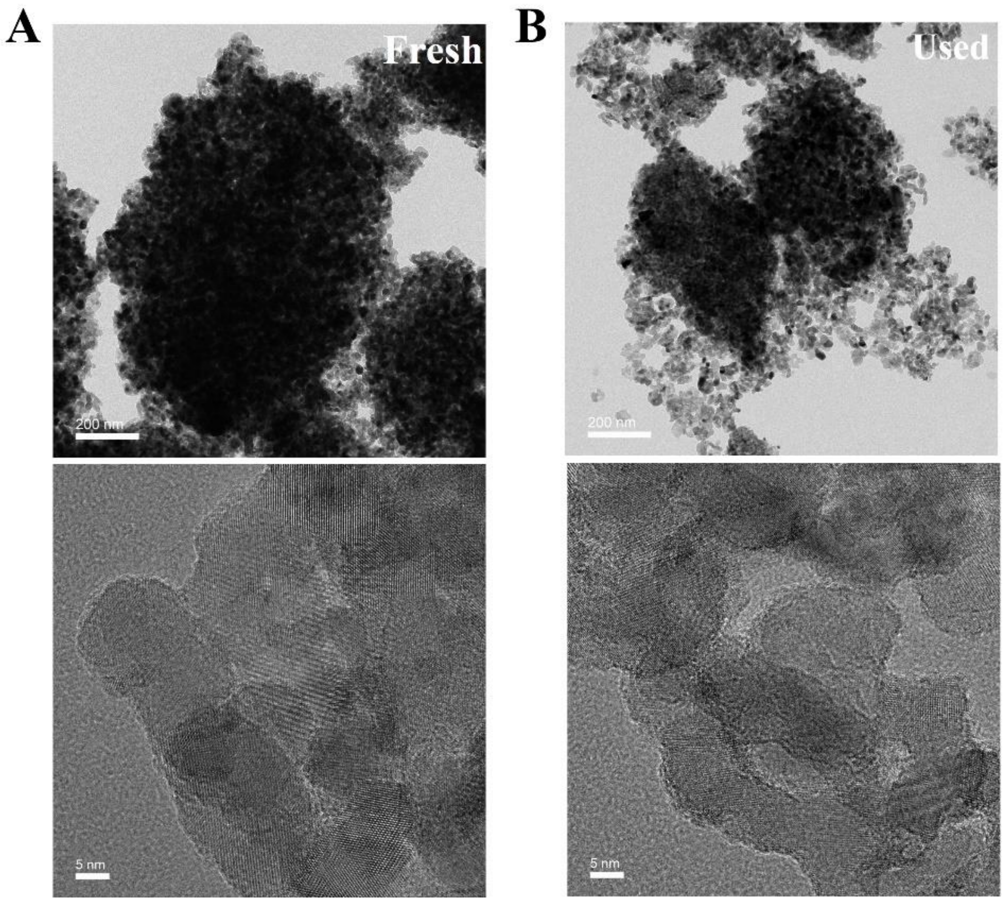

Supplementary Figure 5. The HR-TEM images of (A) fresh and (B) used Cu–Pd/TiO_2 photocatalyst.

The HR-TEM images reveal that both fresh and used Cu–Pd/TiO_2 catalysts consist of nanosized particles uniformly dispersed on the TiO_2 matrix. After catalytic reaction, the used catalyst preserves the nanoscale morphology without obvious particle growth or aggregation. The absence of significant structural degradation further confirms the high stability of Cu–Pd/TiO_2 during reaction.

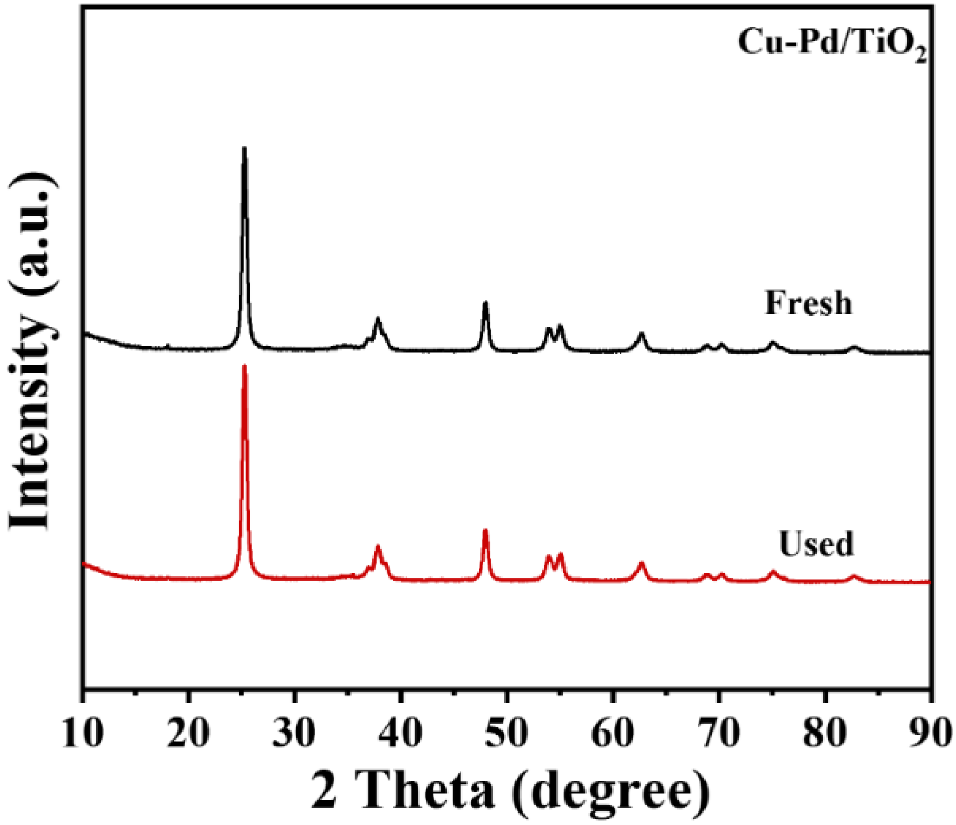

Supplementary Figure 6. XRD patterns of fresh and used Cu–Pd/TiO_2 photocatalyst.

The XRD patterns of fresh and used Cu–Pd/TiO_2 catalysts are presented in Supplementary Figure 6. Both samples show characteristic diffraction peaks assigned to the anatase TiO_2 phase, indicating that TiO_2 remains as the dominant crystalline structure. No obvious diffraction peaks corresponding to Cu or Pd species are detected, which may be attributed to their low loading amount, high dispersion, or small particle size. After reaction, the diffraction pattern of the used catalyst remains almost unchanged, suggesting that the crystalline structure of the catalyst is well preserved during photocatalysis.

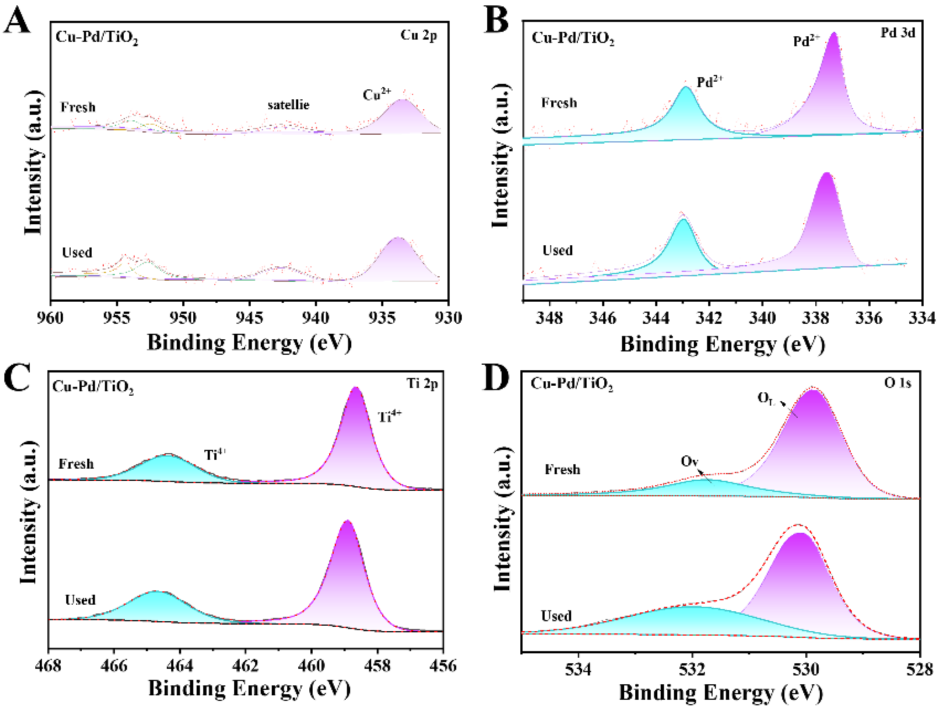

Supplementary Figure 7. XPS spectra of (A) Cu 2p, (B) Pd 3d, (C) Ti 2p and (D) O 1s of fresh and used Cu–Pd/TiO_2 photocatalyst.

The Cu 2p XPS spectra in Supplementary Figure 7A show characteristic Cu species on the Cu–Pd/TiO_2 catalyst. The Cu $2p_{3/2}$ peak located around 933–935 eV can be attributed to Cu^{2+} species. After reaction, the preservation of Cu signals indicates that Cu species remain anchored on TiO_2 without significant loss. The Pd 3d spectra in Supplementary Figure 7B display two characteristic peaks corresponding to Pd $3d_{5/2}$ and Pd $3d_{3/2}$. The peaks can be assigned to oxidized Pd^{2+} species. After catalytic reaction, the Pd signals remain detectable with only minor variations, indicating that Pd species possess good stability. The Ti 2p spectra in Supplementary Figure 7C exhibit two typical peaks corresponding to Ti $2p_{3/2}$ and Ti $2p_{1/2}$, which are assigned to Ti^{4+} species in TiO_2. No obvious change is observed after reaction, suggesting that the TiO_2 framework remains stable. The maintained Ti^{4+} state indicates that the support structure is not significantly reduced or damaged during reaction. The O 1s spectra in Supplementary Figure 7D can be deconvoluted into lattice oxygen species and oxygen vacancies. Compared with the fresh catalyst, the used sample shows variation in the relative contribution of oxygen vacancies.

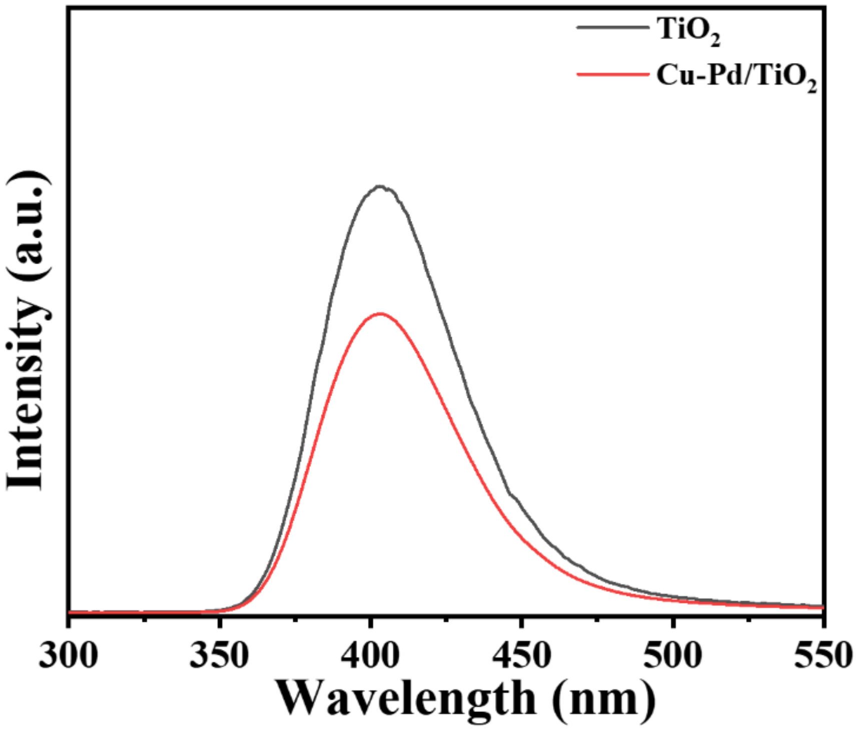

Supplementary Figure 8. PL spectra of TiO_2 and Cu–Pd/TiO_2 photocatalyst.

The PL spectra in Supplementary Figure 8 indicates that Cu–Pd/TiO_2 exhibits the highest charge separation efficiency compared with TiO_2.

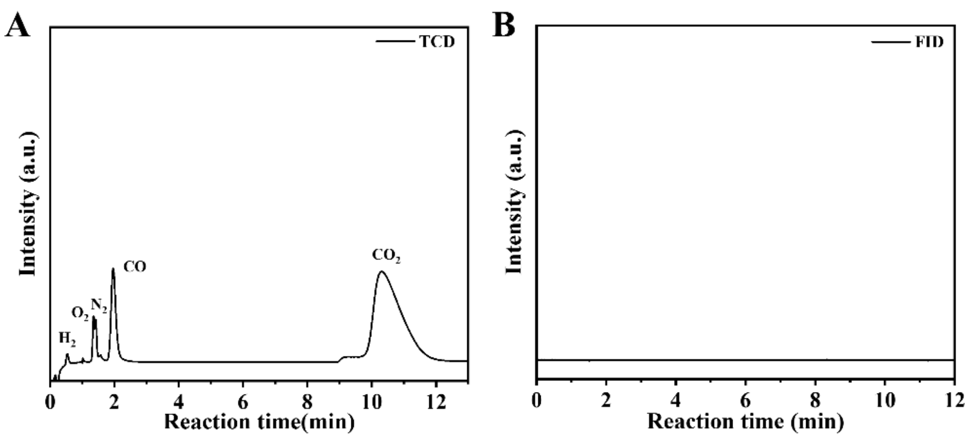

Supplementary Figure 9. (A) TCD chromatogram of H_2 and CO and (B) FID chromatogram of hydrocarbon products generated from reduction of CO_2 and H_2O catalysed by the collaboration of Cu–Pd/TiO_2 catalyst, DBD plasma and light.

To investigate the formation of possible carbon-containing products, the reactor effluent was simultaneously analysed using both TCD and FID detectors. As shown in Supplementary Figure 9, no detectable peaks corresponding to methane, methanol, ethanol, ethane, or other hydrocarbons or oxygenated compounds were observed in the FID chromatograms within the detection limit of the GC system. Therefore, under the present experimental conditions, CO was identified as the only detectable carbon-containing product.

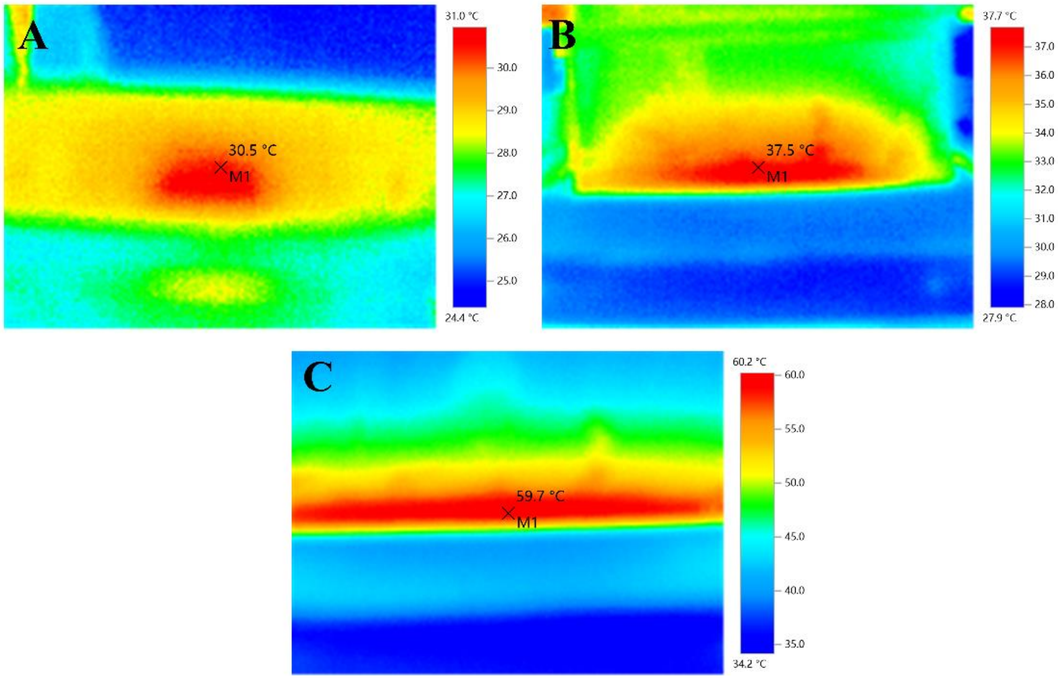

Supplementary Figure 10. Infrared thermal images of reactor during reaction under (A) non-reacting conditions, (B) light-only conditions and (C) plasma−light coupling conditions.

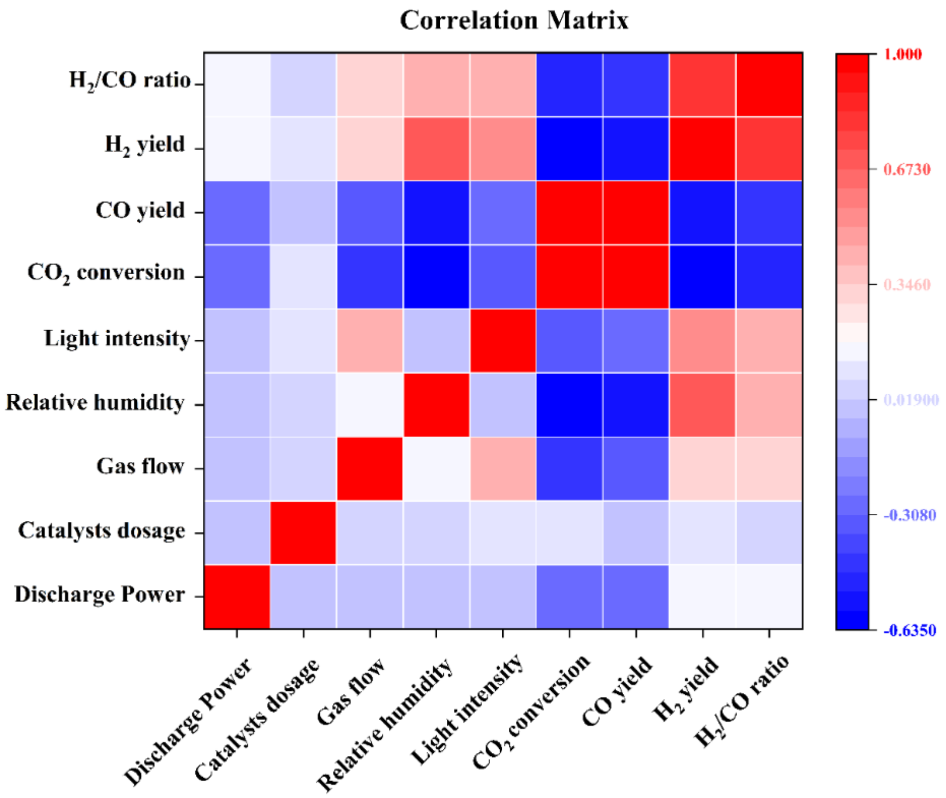

Supplementary Figure 11. The correlation matrix graph.

To obtain an initial overview of the relationships among the operating variables and reaction outputs, a Pearson correlation matrix was constructed in Supplementary Figure 11. CO_2 conversion showed a strong positive correlation with CO yield, indicating that CO formation is closely associated with CO_2 conversion in this system. In contrast, CO_2 conversion and CO yield were negatively correlated with H_2 yield and H_2/CO ratio, suggesting a competitive relationship between CO_2 reduction toward CO and hydrogen evolution. Relative humidity was positively correlated with H_2 yield and H_2/CO ratio but negatively correlated with CO_2 conversion and CO yield, indicating that increasing water content tends to shift the reaction toward H_2 formation. It should be noted that the correlation matrix only reflects pairwise linear relationships and cannot fully describe nonlinear or coupled effects among variables. For example, discharge power and light intensity may exhibit optimal operating windows rather than monotonic effects, which can lead to weak linear correlations despite their strong influence on reaction performance. Therefore, the correlation analysis was used only as a preliminary description of the dataset, while PFI, SHAP analysis, and response-trend analysis were further employed to reveal nonlinear variable effects and multi-objective competition in the plasma-coupled photocatalytic system.

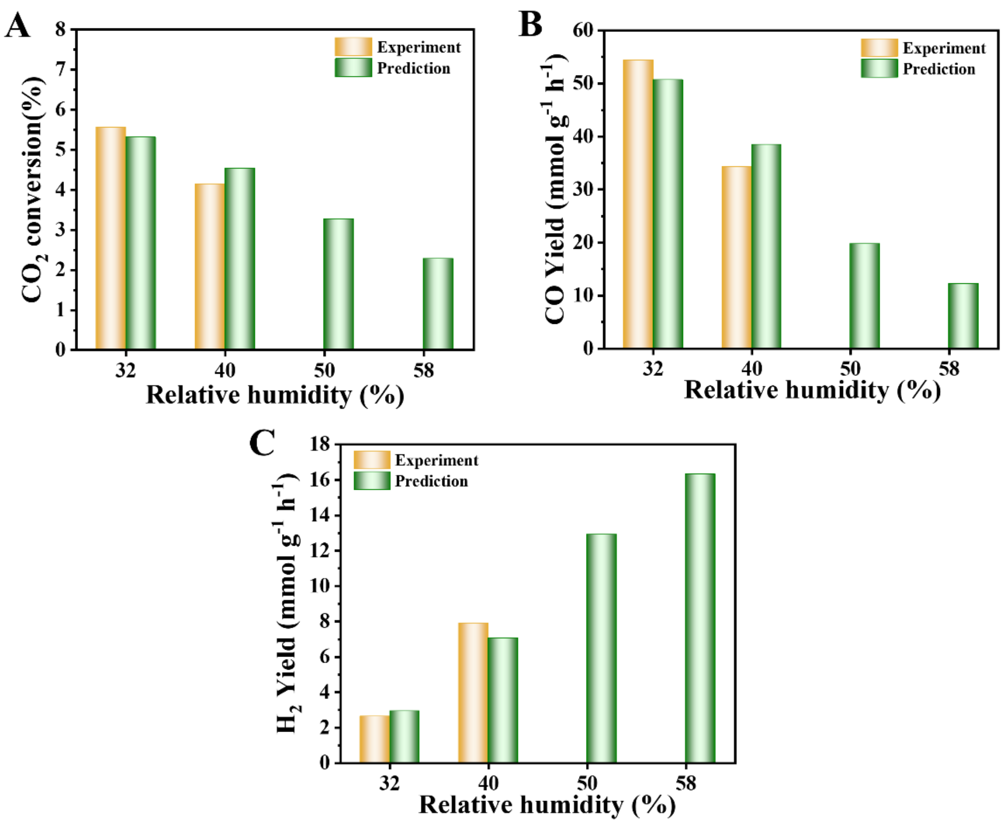

Supplementary Figure 12. Correlation between hybrid model prediction and experimental data for the effect of relative humidity on the plasma-photocatalytic CO_2 and H_2O conversion reaction performance (A) CO_2 conversion, (B) CO yield and (C) H_2 yield (Discharge power: 50 W, light intensity: 1000 mW cm^{-2}, gas flow: 20 mL min^{-1}, catalyst dosage: 60 mg).

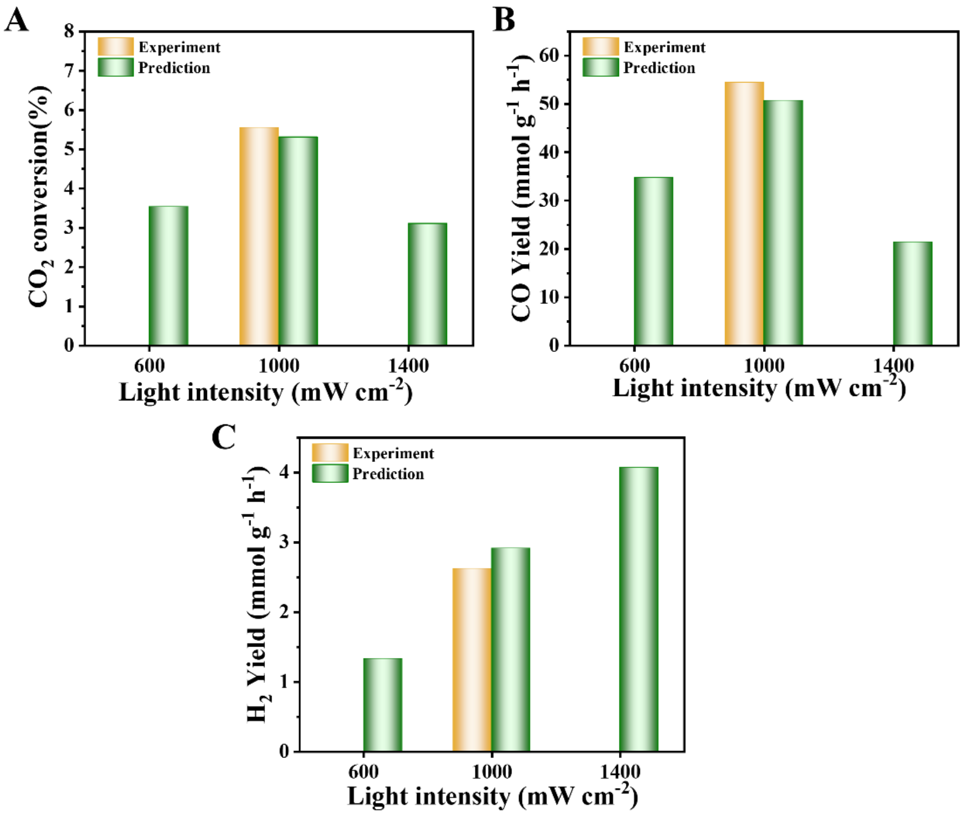

Supplementary Figure 13. Correlation between hybrid model prediction and experimental data for the effect of light intensity on the plasma-photocatalytic CO_2 and H_2O conversion reaction performance (A) CO_2 conversion, (B) CO yield and (C) H_2 yield (Discharge power: 50 W, relative humidity: 32 %, gas flow: 20 mL min^{-1}, catalyst dosage: 60 mg).

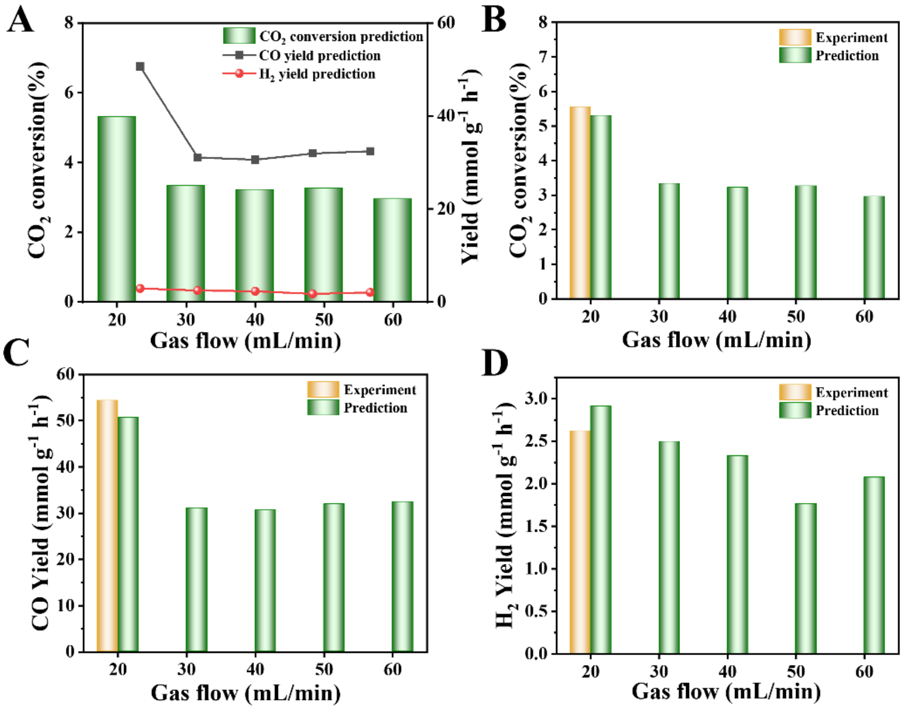

Supplementary Figure 14. Predicted effects of (A) gas flow on the plasma-photocatalytic CO_2 and H_2O conversion reaction performance. Correlation between hybrid model prediction and experimental data for the effect of gas flow on the plasma-photocatalytic CO_2 and H_2O conversion reaction performance (B) CO_2 conversion, (C) CO yield and (D) H_2 yield (Discharge power: 50 W, light intensity: 1000 mW cm^{-2}, relative humidity: 32 %, catalyst dosage: 60 mg).

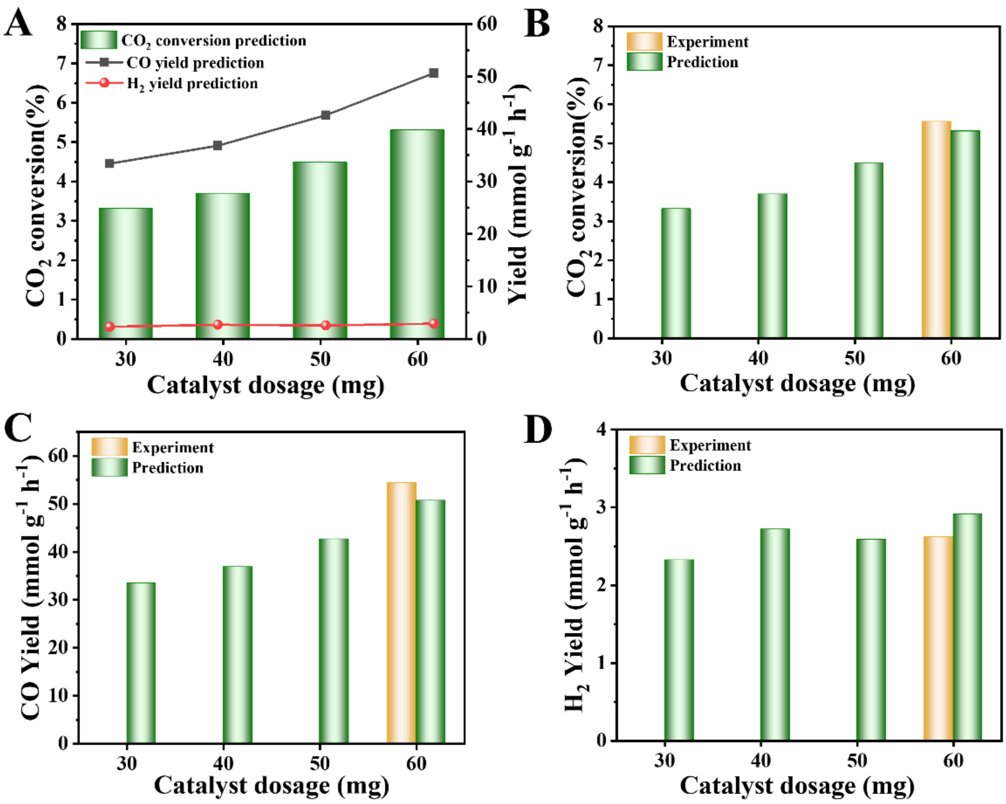

Supplementary Figure 15. Predicted effects of (A) catalyst dosage on the plasma-photocatalytic CO_2 and H_2O conversion reaction performance. Correlation between hybrid model prediction and experimental data for the effect of catalyst dosage on the plasma-photocatalytic CO_2 and H_2O conversion reaction performance (B) CO_2 conversion, (C) CO yield and (D) H_2 yield (Discharge power: 50 W, light intensity: 1000 mW cm^{-2}, relative humidity: 32 %, gas flow: 20 mL min^{-1}).

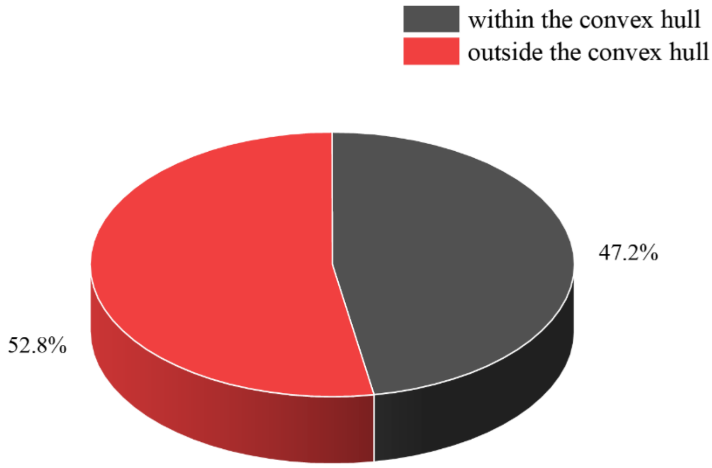

Supplementary Figure 16. Distribution of the 100,000 generated candidate conditions inside and outside the convex hull of the SPXY training set.

Supplementary Table 1. The comparison of different catalysts under only-plasma and plasma-light conditions (Discharge power: 60 W, catalysts dose: 30 mg, gas flow: mL min^{-1}, relative humidity 50%, light intensity: 1000 mW cm^{-2})

	Only plasma conditions			Plasma + light conditions		
Catalysts	**CO_2 conversion (%)**	**CO yield (mmol g^{-1} h^{-1})**	**H_2 yield (mmol g^{-1} h^{-1})**	**CO_2 conversion (%)**	**CO yield (mmol g^{-1} h^{-1})**	**H_2 yield (mmol g^{-1} h^{-1})**
CeO_2	0.58±0.08	5.82±0.72	15.34±2.10	0.82±0.10	8.63±1.04	12.52±1.63
Al_2O_3	0.50±0.07	4.91±0.66	13.80±1.85	0.43±0.06	4.12±0.58	11.96±1.52
ZSM-5	0.38±0.05	3.55±0.49	10.70±1.36	0.40±0.06	3.71±0.52	9.95±1.29
TiO_2	0.76±0.09	7.86±0.92	16.28±2.24	1.05±0.13	11.42±1.35	13.03±1.68
Cu/TiO_2	1.07±0.15	10.95±1.62	7.12±0.96	1.33±0.18	13.82±2.14	6.96±0.94
Pd/TiO_2	1.24±0.17	11.50±1.86	8.39±1.12	1.06±0.15	10.81±1.71	10.60±1.48
Cu–Pd/TiO_2	1.40±0.26	13.93±1.94	24.93±3.28	2.86±0.54	28.52±3.96	18.51±2.93

Supplementary Table 2. Carbon balance of 20 independently experimental runs

No.	Carbon balance (%)
1	99.93±0.12
2	99.87±0.15
3	99.83±0.21
4	99.90±0.10
5	99.77±0.25
6	99.80±0.10
7	99.73±0.31
8	99.77±0.15
9	99.90±0.17
10	99.80±0.26
11	99.87±0.12
12	99.77±0.21
13	99.83±0.12
14	99.70±0.20
15	99.80±0.17
16	99.87±0.06
17	99.70±0.30
18	99.87±0.23
19	99.73±0.21
20	99.83±0.15

Supplementary Table 3. Comparison of other state-of-the-art photocatalysts

Catalyst	CO yield (μmol g^{-1} h^{-1})	H_2 yield (μmol g^{-1} h^{-1})	Syngas H_2/CO ratio	Reference
CIS/Co-PBA/NaY-5	306.19	1152.29	3.76:1	[3]
30% ZIF-BT	2486.4	3495.0	1.41:1	[4]
150TiO_2/CN	6200	1900	0.31:1	[5]
CdS/$BiVO_4$@T-COF	183.8	269.8	1.47:1	[6]
$Zn_{0.8}Cd_{0.2}S$	680	1020	1.5:1	[7]
CdS_{1-x}-M	96.18	569.12 [1]	6:1	[8]
3 wt% Ni_2P/CdS	50.6	115	2.27:1	[9]
Cu–Pd/TiO_2	56420	53710	0.022:1-53.71:1	This work

Supplementary Table 4. Experimental dataset of plasma-coupled photocatalysis CO_2 and H_2O conversion reaction

NO	Discharge power (W)	Catalysts dose (mg)	Gas flow (mL min^{-1})	Relative humidity (%)	Light intensity (mW cm^{-2})
1	40	60	20	32	1000
2	70	30	40	58	1400
3	30	30	60	32	1400
4	70	50	20	58	600
5	60	30	20	32	600
6	30	60	60	58	1400
7	50	60	30	40	1400
8	30	30	50	58	600
9	30	50	50	40	1000
10	70	40	60	40	1400
11	70	50	40	32	600

12	70	60	30	50	1400
13	30	30	40	58	1400
14	60	30	30	50	1000
15	30	60	40	50	600
16	60	60	20	40	1000
17	70	60	50	58	1000
18	40	40	30	58	1000
19	70	60	60	58	1400
20	60	40	50	32	1000
21	70	30	50	58	600
22	30	30	20	40	600
23	50	60	40	40	600
24	70	50	30	32	1400
25	30	50	30	32	1400
26	70	30	30	50	1000
27	40	40	50	32	1000
28	40	60	50	58	1000
29	30	60	30	50	1400
30	70	30	20	40	600
31	70	60	20	40	1000
32	40	50	20	58	600
33	30	60	20	40	1000
34	40	30	20	32	600
35	30	30	30	50	1000
36	60	50	60	50	1400
37	60	60	50	50	1000
38	50	40	20	50	600
39	30	50	40	32	600
40	50	60	30	50	1400
41	70	50	50	40	1000
42	60	60	40	50	600
43	60	30	60	32	1400
44	40	40	60	40	1400
45	60	40	30	58	1000
46	40	60	50	50	1000
47	50	60	60	58	1400
48	30	50	60	50	1400
49	30	60	30	40	1400

50	70	60	30	40	1400
51	70	60	40	40	600
52	50	50	30	32	1400
53	50	30	40	58	1400
54	60	50	50	40	1000
55	60	50	40	32	600
56	30	40	20	50	600
57	30	60	40	40	600
58	70	40	20	50	600
59	70	60	40	50	600
60	70	40	50	32	1000
61	70	60	20	32	1000
62	30	60	50	50	1000
63	50	30	50	58	600
64	60	50	20	58	600
65	30	60	20	32	1000
66	60	30	20	40	600
67	60	30	40	58	1400
68	40	50	60	50	1400
69	50	50	50	40	1000
70	70	30	60	32	1400
71	60	40	60	40	1400
72	70	60	50	50	1000
73	60	60	20	32	1000
74	50	40	50	32	1000
75	60	40	20	50	600
76	50	30	20	40	600
77	40	60	30	50	1400
78	30	40	30	58	1000
79	60	50	30	32	1400
80	40	30	30	50	1000
81	60	60	40	40	600
82	40	50	40	32	600
83	70	40	30	58	1000
84	30	40	50	32	1000
85	40	60	20	40	1000
86	60	60	30	50	1400
87	30	30	20	32	600

88	60	60	60	58	1400
89	70	30	20	32	600
90	70	50	60	50	1400
91	50	30	20	32	600
92	40	30	40	58	1400
93	40	60	30	40	1400
94	50	50	60	50	1400
95	50	60	50	58	1000
96	50	40	30	58	1000
97	30	50	20	58	600
98	30	60	50	58	1000
99	30	40	60	40	1400
100	40	30	20	40	600
101	40	60	40	40	600
102	40	40	20	50	600
103	40	60	40	50	600
104	40	30	50	58	600
105	40	50	50	40	1000
106	40	50	30	32	1400
107	40	30	60	32	1400
108	40	60	60	58	1400
109	50	50	40	32	600
110	50	60	40	50	600
111	50	50	20	58	600
112	50	60	20	32	1000
113	50	60	20	40	1000
114	50	30	30	50	1000
115	50	60	50	50	1000
116	50	30	60	32	1400
117	50	40	60	40	1400
118	60	30	50	58	600
119	60	60	50	58	1000
120	60	60	30	40	1400

Supplementary Table 5. Comparison of hybrid model prediction and experimental results

No	Model Prediction			Actual experiment		
	CO_2 conversion (%)	CO yield (mmol g^{-1} h^{-1})	H_2 yield (mmol g^{-1} h^{-1})	CO_2 conversion (%)	CO yield (mmol g^{-1} h^{-1})	H_2 yield (mmol g^{-1} h^{-1})
1	5.38	53.43	2.68	5.52±0.73	56.42±6.10	2.21±0.26
2	0.45	0.78	53.47	0.43±0.06	1.00±0.14	53.71±5.19
3	1.59	11.76	4.19	1.54±0.14	10.31±1.28	4.00±0.54
4	0.87	0.99	12.75	0.85±0.11	1.33±0.15	13.20±1.41
5	3.10	28.69	1.92	3.17±0.30	27.25±2.68	2.25±0.36
6	0.72	1.32	32.67	0.81±0.09	1.00±0.12	32.93±4.07
7	1.98	8.86	14.83	2.15±0.20	9.08±0.82	15.37±2.03
8	1.04	3.99	9.97	1.13±0.13	4.25±0.55	9.68±1.20
9	3.23	31.16	6.94	3.25±0.30	31.49±3.42	7.50±0.62
10	0.75	2.05	11.95	0.70±0.12	2.48±0.29	12.12±1.08
11	1.97	10.62	1.74	2.09±0.25	9.33±1.08	1.38±0.20
12	0.64	2.11	40.27	0.57±0.09	1.66±0.17	41.87±5.01
13	0.56	3.26	39.41	0.39±0.06	3.30±0.42	40.47±4.14
14	2.57	24.28	18.07	2.86±0.54	28.52±3.96	18.51±2.93
15	1.90	9.31	7.84	2.00±0.19	9.91±0.81	8.32±0.97
16	4.09	31.13	7.40	4.17±0.51	31.92±3.55	6.12±0.60
17	0.93	2.36	25.63	0.83±0.11	2.73±0.42	26.47±3.74
18	2.01	12.28	18.74	2.04±0.20	11.99±1.12	18.82±2.62
19	0.22	0.81	50.79	0.28±0.04	1.00±0.12	51.99±5.88
20	3.31	35.88	2.60	3.26±0.40	36.93±2.92	2.37±0.33
21	0.55	0.99	12.82	0.55±0.07	1.74±0.25	13.12±1.88
22	2.82	22.96	3.87	2.61±0.25	21.00±2.33	4.58±0.52
23	2.94	21.09	4.71	3.05±0.42	21.14±2.54	5.87±0.57
24	1.35	3.64	6.64	1.28±0.13	3.62±0.46	6.66±0.79
25	2.42	14.03	4.04	2.32±0.25	12.93±1.18	4.79±0.69
26	1.35	8.91	18.20	1.17±0.14	5.28±0.46	18.11±1.49
27	4.01	48.52	2.56	4.06±0.58	52.41±5.30	3.21±0.42
28	1.67	7.99	16.18	1.54±0.14	4.99±0.44	16.92±2.43
29	1.43	5.39	24.69	1.68±0.24	6.59±0.72	25.02±3.39
30	1.66	9.78	4.00	1.78±0.20	10.48±1.16	3.70±0.41

31	2.53	13.20	8.12	2.31±0.31	10.95±1.14	9.24±0.94
32	1.53	9.82	8.57	1.33±0.16	8.26±0.66	7.89±1.09
33	4.57	38.40	7.12	4.57±0.58	38.18±4.81	7.49±0.63
34	3.61	37.84	1.21	3.77±0.47	40.16±4.48	0.88±0.12
35	2.62	24.95	12.11	2.55±0.37	25.47±3.23	11.87±1.69
36	0.81	3.02	32.07	0.69±0.09	2.57±0.31	30.88±3.12
37	2.21	12.01	16.52	2.23±0.23	11.36±1.36	17.51±2.46
38	2.33	16.26	7.02	2.39±0.30	17.01±1.29	5.70±0.51
39	3.18	27.68	1.21	3.20±0.46	26.46±3.22	0.80±0.12
40	1.30	5.86	32.91	1.25±0.12	8.29±1.09	35.62±4.72
41	2.16	14.27	7.32	2.18±0.24	13.02±1.17	7.41±0.71
42	1.95	8.82	9.09	1.97±0.19	8.83±0.88	8.63±1.04
43	1.28	7.66	4.13	1.19±0.17	6.93±0.61	4.34±0.49
44	1.35	6.25	12.44	1.31±0.13	5.40±0.72	12.52±1.78
45	1.64	9.90	25.22	1.56±0.17	9.16±1.11	26.11±2.45
46	2.55	15.64	12.23	2.64±0.28	17.84±1.61	10.51±0.86
47	0.44	1.45	37.24	0.28±0.04	1.00±0.16	36.88±4.65
48	0.97	4.56	24.67	1.06±0.12	6.09±0.60	23.91±2.41
49	1.81	8.30	11.00	1.68±0.17	7.29±0.77	10.38±0.97
50	1.17	3.30	16.93	1.32±0.16	4.83±0.61	16.58±2.14
51	1.48	5.47	4.81	1.29±0.16	4.26±0.42	4.07±0.58
52	2.64	13.56	3.72	2.77±0.38	12.63±1.57	1.36±0.20
53	0.90	3.74	40.77	0.91±0.15	4.55±0.55	38.79±4.95
54	3.03	26.98	7.29	2.98±0.40	28.57±3.42	6.98±0.87
55	3.10	25.13	1.52	3.02±0.38	24.54±2.53	0.80±0.12
56	2.18	12.76	6.56	2.28±0.29	12.49±1.51	6.60±0.83
57	2.51	18.10	3.61	2.41±0.28	17.90±1.45	2.66±0.29
58	1.28	3.26	9.38	1.41±0.14	3.37±0.28	8.75±1.02
59	1.03	1.40	11.15	0.91±0.12	2.15±0.26	12.89±1.23
60	2.18	17.73	2.53	2.07±0.27	14.09±1.36	1.73±0.24
61	2.90	16.65	3.56	2.96±0.34	17.10±1.65	2.59±0.30
62	2.11	10.52	12.81	1.92±0.23	8.68±1.09	13.62±1.21
63	1.19	5.12	9.63	1.08±0.10	3.69±0.40	9.75±1.04
64	1.67	7.04	11.51	1.80±0.20	6.38±0.61	11.82±1.50
65	5.03	47.36	2.93	5.01±0.68	46.69±4.33	3.16±0.38
66	2.78	21.28	4.10	2.69±0.31	20.94±2.58	3.75±0.48
67	0.91	4.06	48.34	1.10±0.12	4.94±0.56	49.32±5.14
68	0.82	3.11	29.30	0.65±0.08	1.46±0.21	29.88±2.58

69	3.39	31.58	6.69	3.64±0.31	33.87±3.03	7.17±1.03
70	0.49	2.28	5.12	0.50±0.08	2.32±0.35	5.26±0.62
71	1.34	4.74	10.48	1.44±0.18	4.69±0.40	9.86±1.30
72	1.51	4.60	17.93	1.66±0.19	5.27±0.52	17.12±1.52
73	4.49	36.71	3.54	4.54±0.40	37.28±3.29	4.42±0.39
74	3.78	42.98	2.39	3.86±0.45	44.01±3.94	2.83±0.30
75	2.07	12.43	8.54	1.91±0.19	12.18±1.01	9.89±1.00
76	3.03	27.17	3.66	3.02±0.41	28.72±3.85	3.70±0.31
77	1.26	5.43	29.50	1.18±0.13	2.46±0.39	28.88±2.98
78	1.87	10.26	13.37	1.94±0.28	10.56±1.11	11.52±1.33
79	2.33	11.42	5.37	2.36±0.21	12.63±1.17	7.06±0.66
80	2.95	27.87	13.91	3.13±0.34	28.82±3.42	13.96±1.16
81	2.58	16.28	4.41	2.63±0.24	15.39±1.31	3.98±0.46
82	3.47	31.57	1.93	3.49±0.46	33.04±4.12	2.90±0.38
83	1.08	3.39	26.44	1.07±0.11	4.43±0.41	27.04±2.49
84	3.76	44.86	2.21	3.88±0.52	45.45±4.20	2.43±0.41
85	4.87	43.61	6.94	4.95±0.72	43.75±5.83	7.49±0.98
86	1.14	5.39	33.99	1.06±0.15	4.12±0.37	30.88±3.02
87	3.39	33.80	1.34	3.44±0.30	34.43±2.68	1.09±0.18
88	0.43	2.13	42.59	0.35±0.05	2.70±0.31	42.70±4.03
89	1.79	14.33	1.86	1.66±0.24	14.16±1.26	1.77±0.25
90	0.44	1.87	36.29	0.49±0.06	3.24±0.41	36.04±3.76
91	3.54	36.04	1.53	3.48±0.45	35.54±4.78	1.84±0.26
92	0.82	3.24	41.36	0.82±0.09	1.20±0.14	42.20±4.86
93	1.79	9.01	13.54	1.61±0.21	9.89±0.93	13.88±1.67
94	0.93	2.24	29.77	1.07±0.10	1.00±0.12	30.78±3.60
95	1.61	8.48	18.39	1.72±0.15	9.13±0.75	17.11±2.28
96	1.85	10.82	21.94	1.79±0.23	10.56±1.07	21.84±3.04
97	1.39	7.04	7.99	1.61±0.18	9.45±1.18	10.56±1.35
98	1.35	3.22	15.68	1.55±0.21	6.75±0.68	13.35±1.19
99	1.30	7.32	10.32	1.16±0.14	6.76±0.91	12.00±1.11
100	3.00	27.61	3.49	2.86±0.27	26.00±2.22	4.32±0.38
101	2.87	21.06	4.06	2.87±0.27	20.55±1.75	2.81±0.36
102	2.31	16.18	6.46	2.41±0.34	17.20±1.40	5.56±0.73
103	2.24	11.94	7.45	2.08±0.22	9.33±1.16	8.53±1.10
104	1.15	5.63	9.75	1.05±0.13	1.97±0.20	9.69±1.14
105	3.56	35.10	6.76	3.57±0.51	35.95±2.70	5.41±0.67
106	2.52	14.64	3.92	2.05±0.27	12.74±1.70	5.63±0.52

107	1.65	11.77	4.64	1.31±0.12	8.45±0.84	6.58±0.79
108	0.43	0.99	35.12	0.46±0.06	1.67±0.23	36.15±3.18
109	3.47	31.34	1.89	3.31±0.30	30.00±2.98	2.11±0.23
110	2.29	12.27	8.12	2.15±0.31	12.54±1.51	8.72±0.82
111	1.75	9.88	9.50	1.55±0.20	5.08±0.53	7.68±0.79
112	5.06	48.03	3.01	5.55±0.52	54.39±6.76	2.62±0.42
113	4.61	40.31	6.86	4.14±0.52	34.28±3.08	7.89±0.72
114	2.91	26.75	15.53	3.30±0.32	31.72±3.93	14.11±1.30
115	2.48	14.42	13.67	2.46±0.33	14.34±1.92	10.84±1.25
116	1.68	10.28	3.65	1.43±0.21	7.57±0.79	2.99±0.47
117	1.50	5.13	10.86	1.41±0.13	6.10±0.54	12.62±1.65
118	1.10	4.67	11.40	0.81±0.09	3.56±0.43	13.23±1.19
119	1.42	7.29	22.83	0.88±0.15	4.80±0.47	26.06±2.46
120	1.85	7.80	14.27	1.51±0.22	4.89±0.40	13.58±1.44

Supplementary Table 6. 10 sets unseen reaction conditions

No.	**Discharge Power (W)**	**Catalysts Dosage (mg)**	**Gas Flow (mL min^{-1})**	**Relative Humidity (%)**	**Light Intensity (mW cm^{-2})**
1	30	60	30	46	650
2	65	30	60	40	1350
3	70	55	20	54	1300
4	30	35	30	56	1400
5	65	30	25	36	650
6	30	30	60	46	650
7	30	60	60	40	1400
8	60	55	60	56	850
9	45	45	20	33	1300
10	35	30	20	53	600

Supplementary Table 7. Comparison of hybrid model prediction and experimental results over 10 sets unseen reaction conditions

No.	Model Prediction			Actual experiment		
	CO_2 conversion (%)	CO yield (mmol g^{-1} h^{-1})	H_2 yield (mmol g^{-1} h^{-1})	CO_2 conversion (%)	CO yield (mmol g^{-1} h^{-1})	H_2 yield (mmol g^{-1} h^{-1})
1	2.1	12.65	6.19	2.43±0.08	13.87±0.34	6.65±0.21
2	0.94	3.51	11.38	1.27±0.05	5.71±0.21	12.36±0.20
3	0.71	1.65	27.18	1.06±0.05	1.39±0.08	30.38±0.63
4	0.95	3.71	30.97	0.87±0.04	2.78±0.10	33.16±0.78
5	2.65	22.57	2.3	3.00±0.07	20.00±0.31	3.20±0.10
6	1.49	8	7.47	1.19±0.05	10.02±0.18	8.81±0.21
7	1.24	7.23	10.99	1.12±0.04	9.81±0.20	12.05±0.23
8	1.32	9.11	14.28	1.59±0.06	8.14±0.18	15.82±0.25
9	2.92	20.68	3.72	3.10±0.07	19.27±0.38	3.00±0.11
10	1.97	11.78	6.78	1.70±0.06	13.26±0.25	8.89±0.21

Supplementary Table 8. Performance of models of absolute production rate

Output	Dataset	R^2	MAE	RMSE
CO yield (mmol h^{-1})	Train	0.992	0.046	0.062
	Test	0.952	0.119	0.162
H_2 yield (mmol h^{-1})	Train	0.992	0.046	0.062
	Test	0.960	0.071	0.093

The absolute CO and H_2 production rates were calculated by multiplying the mass-normalized yield by the catalyst mass in grams: absolute production rate = mass-normalized yield × catalyst mass. CO_2 conversion was retained in its original percentage form because it was not normalized by catalyst mass. The same input variables, SPXY data split, and hybrid modelling procedure were used for the additional models. The results are summarized in Supplementary Table 8. The test-set R^2 values of the absolute-rate models were 0.952 for CO and 0.960 for H_2, which were comparable to those of the corresponding mass-normalized yield models (0.950

and 0.954 in Figure 3B and C, respectively). These results indicate that the main predictive relationships were not solely caused by catalyst-mass normalization. Because the mass-normalized and absolute outputs have different units, their MAE and RMSE values should not be directly compared. The mass-normalized yields were retained as the primary outputs for the main analysis.

Supplementary Table 9. Model-predicted low–high pairwise interaction contrasts among the operating variables for CO_2 conversion, CO yield and H_2 yield

Variable pair	**CO_2 conversion (%)**	**CO yield (mmol g^{-1} h^{-1})**	**H_2 yield (mmol g^{-1} h^{-1})**
Discharge power × catalyst dosage	0.43	8.15	0.18
Discharge power × gas flow	0.78	7.66	−1.14
Discharge power × relative humidity	0.91	18.48	10.91
Discharge power × light intensity	0.34	4.44	2.31
Catalyst dosage × gas flow	−1.16	−7.21	−2.24
Catalyst dosage × relative humidity	0.11	1.71	−1.62
Catalyst dosage × light intensity	−0.51	−2.30	−0.38
Gas flow × relative humidity	−0.14	−4.33	0.79
Gas flow × light intensity	0.30	1.38	1.69
Relative humidity × light intensity	0.25	11.04	27.44

The low–high screening results in Supplementary Table 9 showed that the conditional effects depended on both the selected variable pair and the reaction output. The discharge power–relative humidity pair exhibited positive interaction contrasts for CO_2 conversion, CO yield, and H_2 yield, with values of 0.91%, 18.48 mmol g^{-1} h^{-1}, and 10.91 mmol g^{-1} h^{-1}, respectively. This indicates that the effect of discharge power depends on the humidity level, possibly because plasma energy input and water loading jointly influence the reaction environment. The relative humidity–light intensity pair showed the strongest conditional interaction for H_2 yield, with an interaction contrast of 27.44 mmol g^{-1} h^{-1}, compared with 11.04 mmol g^{-1} h^{-1} for CO yield and 0.25% for CO_2 conversion. This output-dependent behaviour may reflect the coupled influence of water availability and photocatalyst excitation on hydrogen formation. The formation of H_2 may be more sensitive to the combined effect of these two variables in this P^2CR system. The catalyst dosage–gas flow rate pair produced negative interaction contrasts for all three outputs, including −1.16% for CO_2 conversion and −7.21 mmol g^{-1} h^{-1} for CO yield. This behaviour may be associated with the shortened residence time at higher flow rates, which can limit the utilization of additional catalytic surface sites. The discharge power–gas flow rate and gas flow rate–relative humidity pairs exhibited different interaction directions among the three outputs. This observation is consistent with the competing effects of plasma energy input, residence time, reactant throughput, and water-vapor supply. Overall, these results indicate that the operating variables form a coupled input space and that the effect of one variable can depend on the level of another. The interaction contrasts represent model-predicted conditional relationships and should not be interpreted as direct evidence of specific elementary reaction mechanisms.

Supplementary Table 10. Recommended reaction conditions of trained hybrid model with H_2/CO target of 1 and 2

H_2/CO target	Discharge Power (W)	Catalysts Dose (mg)	Gas Flow (mL/min)	Relative Humidity (%)	Light Intensity (mW cm^{-2})
1	44	33	35	51	1121
2	57	39	34	54	1119

Supplementary Table 11. Comparison of hybrid model prediction and experimental results over recommended reaction conditions with H_2/CO target of 1 and 2

H_2/CO target	Model prediction				Experimental results			
	CO_2 conversion	CO yield	H_2 yield	H_2/CO	CO_2 conversion	CO yield	H_2 yield	H_2/CO
1	2.64	20.56	21.49	1.05	2.75±0.02	21.99±1.18	23.29±1.03	1.06±0.03
2	2.13	13.15	26.32	2.00	2.25±0.03	14.26±0.51	28.33±1.14	1.99±0.07

Supplementary Table 12. CO productivity per plasma power over recommended reaction conditions with H_2/CO target of 1 and 2

H_2/CO target	Power (W)	Catalyst dosage (g)	CO productivity per plasma power (mmol kWh^{-1})
1	44	0.033	16.5±0.9
2	57	0.039	9.8±0.3

To provide an energy-related descriptor for the recommended conditions, the CO productivity normalized by plasma discharge power was calculated as

$$CO_{power-normalized} = \frac{Y_{CO} \times m_{catalyst}}{P} \quad (4)$$

Y_{CO} is the experimentally measured CO yield (mmol g^{-1} h^{-1}), $m_{catalyst}$ is the catalyst mass (g), and P is the plasma power (kW). The resulting unit is mmol kWh^{-1}.

REFERENCES

1. Phey Phey, M.L., T.A. Tuan Abdullah, U.F. Md Ali, et al., Reverse water gas shift reaction over a Cu/ZnO catalyst supported on regenerated spent bleaching earth (RSBE) in a slurry reactor: the effect of the Cu/Zn ratio on the catalytic activity. *RSC Adv*. **2023**, *13(5)*, 3039-3055. DOI: 10.1039/d2ra07617a.

2. Xie, S., X. Luo, J. Zhao, et al., Synergistic Effect of Copper and Indium Species for Highly Selective CO_2 Hydrogenation to Methanol. *ACS Sustainable Chemistry & Engineering*. **2024**, *12(49)*, 17925-17935. DOI: 10.1021/acssuschemeng.4c08258.

3. Zhang, G., Z. Wang, D. Shi, et al., Rational design of H_2 production sites for achieving photoconversion of CO_2 with H_2O into widely adjustable syngas and highly effective H_2 evolution. *Green Carbon*. **2025**, *3(1)*, 11-21. DOI: 10.1016/j.greenca.2024.07.008.

4. Wang, J., C. Ma, S. Wen, et al., Black TiO_2 coupled with ZIF-67 for enhanced photocatalytic CO_2 reduction to tunable CO/H_2 syngas. *Applied Surface Science*. **2025**, *710*. DOI: 10.1016/j.apsusc.2025.164001.

5. Zhang, J., J. Wu, Y. Zhao, et al., Efficient Photocatalytic CO_2 Reduction to

Syngas with Tunable Ratios Enabled by an S-Scheme TiO_2/CN Heterojunction. *The Journal of Physical Chemistry C*. **2026**, *130(17)*, 6111-6120. DOI: 10.1021/acs.jpcc.6c00924.

6. Fan, Z., Y. Cai, Z. Yang, et al., Integrating CO_2 reduction, H_2O oxidation and H_2 evolution catalysts into a dual S-scheme artificial photosynthetic system for tunable syngas production. *Applied Catalysis B: Environment and Energy*. **2024**, *351*. DOI: 10.1016/j.apcatb.2024.123979.

7. Zhang, Y., M.-Y. Qi, M. Conte, et al., Efficient Photoredox Co-Upcycling of CO_2 and Plastic Waste by Band-Gap-Engineered ZnxCd$_{1-x}$S Catalyst. *ACS Materials Letters*. **2024**, *7(1)*, 359-367. DOI: 10.1021/acsmaterialslett.4c02142.

8. Wang, W., Z. Yang, Q. Yuan, et al., Molecular-Scale Modulation of Surface Hydrogen Dynamics for Enhanced Photocatalytic Syngas Production with Adjustable H_2/CO Ratios over CdS Nanoparticles. *ACS Catalysis*. **2026**. DOI: 10.1021/acscatal.6c00697.

9. Yadav, P., S. Kumar, N. Velankanni, et al., Photocatalytic CO_2 reduction to syngas using nickel phosphide-loaded CdS under visible light irradiation. *Journal of Physics: Energy*. **2024**, *6(2)*. DOI: 10.1088/2515-7655/ad3676.